

Dragonfly-Eye-Inspired Artificial Compound Eyes with Sophisticated Imaging

Zefang Deng, Feng Chen,* Qing Yang,* Hao Bian, Guangqing Du, Jiale Yong, Chao Shan, and Xun Hou

The natural compound eye is a striking imaging device with a wealth of fascinating optical features such as a wide field of view (FOV), low aberration, and high sensitivity. Dragonflies in particular possess large, sophisticated compound eyes that exhibit high resolving power and information-processing capacity. Here, a large-scale artificial compound eye inspired by the unique designs of natural counterparts is presented. The artificial compound eye is created by a high-efficiency strategy that combines single-pulse femtosecond laser wet etching with thermal embossing. These eyes have a macrobase diameter of 5 mm and $\approx 30\,000$ close-packed ommatidia with an average diameter of $24.5\ \mu\text{m}$. Moreover, the optical properties of the artificial compound eyes are investigated; the results confirm that the eye demonstrates advanced imaging quality, an exceptionally wide FOV of up to 140° , and low aberration.

1. Introduction

In nature, many invertebrate eyes exhibit remarkable imaging performance that enables a wide field of view (FOV), minimal aberration, high-sensitivity detection, and fast motion tracking. These compound eyes exhibit a tremendous variety of dimensions, FOVs, sensitivities, and resolving powers, which reflects the evolutionary histories of different types of animals. Many of the more evolutionarily advanced dragonflies possess large, sophisticated compound eyes that are capable of supplying more information. Therefore, they are able to prey on insects or escape from predators with high accuracy even if they approach from behind at high speed.^[1,2] By learning from those natural examples, scientists have copied a wealth of three-dimensional (3D) compound eyes.^[3–8] At the same time, similar man-made optical systems with these characteristics, such as hemispherical digital camera,^[9,10] have attracted a great deal of interest for potential use in surveillance devices, tools for medical examination, and other demanding applications.^[11–16]

Natural compound eyes are typically composed of thousands of small units or ommatidia, which are usually spherically

distributed over portions of the animal's head.^[17] The outermost part of each ommatidium is usually a transparent plano-convex microlens. Therefore, the most prominent characteristic of compound eyes, aside from their protruding shape, is the mosaic of corneal facet lenses; this mosaic perfectly follows the inner organization of the compound eye, which consists of a crystalline cone and subsequent photoreceptor cells.^[11] Recently, a variety of artificial compound eyes that exhibited a relatively wide FOV have been designed and realized.^[18–20] However, some technical obstacles remain to be resolved, including the fact that the lenslet shape, number, dimensions, and fill fraction of

these artificial compound eyes differ greatly from those of the natural ones, which would seriously affect the signal-to-noise ratio and resolving power of the artificial compound eyes.

Because some regions are specialized for particular functions, there are commonly important variations in their size and shape in a single compound eye.^[21–24] For example, the dragonfly's compound eye includes ommatidia with different shapes, which are typically square, hexagonal, or irregular. Moreover, these sophisticated compound eyes possess more ommatidia and exhibit high resolving power.^[25–27] In past decade, several strategies have been adopted to obtain artificial compound eyes, such as laser direct writing,^[28–30] 3D configurations,^[11] or surface wrinkling.^[31] However, these methods hardly control the lenslet geometry and packing due to their intrinsic limitations. All these artificial compound eyes were composed of homogeneously hexagonal microlenses and suffer from a small number of microlenses. Hence, these artificial compound eyes were just functional bionic instead of real life-size devices. In addition, several artificial compound eyes exhibited a low fill fraction, which would seriously degrade their optical performance. It is worthy to mention that high-quality imaging should be closely related to the fact that the surface profiles of lenslets are parabolic instead of spherical. And it is still a challenge to acquire life-size high-quality artificial compound eyes (outer corneal facet lenses) comprising a huge number of parabolic microlenses.

In this work, biologically inspired artificial compound eyes were fabricated by thermomechanical deformation. These artificial compound eyes consist of hexagonal, rectangular, or irregular microlenses with parabolic surface that differ slightly in shape and size, and the average diameter of the ommatidia is about $24.5\ \mu\text{m}$. The total number of ommatidia reaches 30 000,

Dr. Z. Deng, Prof. F. Chen, Prof. Q. Yang, Dr. H. Bian, Dr. G. Du, Dr. J. Yong, Dr. C. Shan, Prof. X. Hou
State Key Laboratory for Manufacturing System Engineering and Key Laboratory of Photonics Technology for Information of Shaanxi Province
School of Electronics and Information Engineering
Xi'an Jiaotong University
Xi'an 710049, P. R. China
E-mail: chenfeng@mail.xjtu.edu.cn; yangqing@mail.xjtu.edu.cn



DOI: 10.1002/adfm.201504941

which is much larger than that of previously reported eyes. The artificial compound eyes were fabricated by a high-throughput technique that combined the ability of single-pulse femtosecond laser wet etching (sp-FLWE) to rapidly produce a large-area concave microlens array with the versatility of thermal embossing. Moreover, high optical performance of the artificial compound eyes was verified, including optical focusing, imaging, and a large FOV with low aberration, using an optical microscopy and intensity scanning system.

2. Results and Discussion

The fabrication process is depicted in Figure 1, and the details are summarized in the Experimental Section. The process has three steps: Fabrication of the master mold and two thermal embossing steps.

The master mold was fabricated by our previously reported sp-FLWE technique, which combines rapidly scanned laser irradiation and subsequent hydrofluoric acid (HF) etching.^[32,33] Figure 2a shows scanning electron microscopy (SEM) pictures of the fabricated microlens arrays (MLAs). We also used laser scanning confocal microscopy (LSCM) to quantify the 3D morphology of the microlenses. The results, which were acquired by repeatedly measuring different zones of the master mold, reveal that the average diameter and sag height of the microlenses were 24.8 and 4.5 μm , and the relative variations were 5.6 and 0.6 μm , respectively.

To achieve a convex MLA, replication based on thermal embossing was implemented. During this process, hundreds of poly(methyl methacrylate) (PMMA) convex MLAs can be replicated from a single master mold without forming observable defects. Figure 2c shows that optically smooth, large-area convex MLAs could be fabricated by thermal embossing. Moreover, the 3D morphology was quantified by LSCM, as shown in Figure 2d. The average diameter and sag height of the convex MLAs were 24.5 and 4.67 μm , respectively. The deformation ratios were $\approx 1\%$, demonstrating that this simple method can realize convex MLAs with relatively high fidelity.

During the fabrication process the shape of the microlenses can be easily controlled by adjusting laser scanning. Actually, we could arbitrarily arrange the distribution of the microlenses with different shapes by setting the start position of the laser scanning. Microlenses with different shapes, including hexagon, square, rectangle, and irregular shape, have been fabricated and replicated (Figure S1, Supporting Information). And the fill factor of the microlenses was close to 100% regardless of the distribution of array.

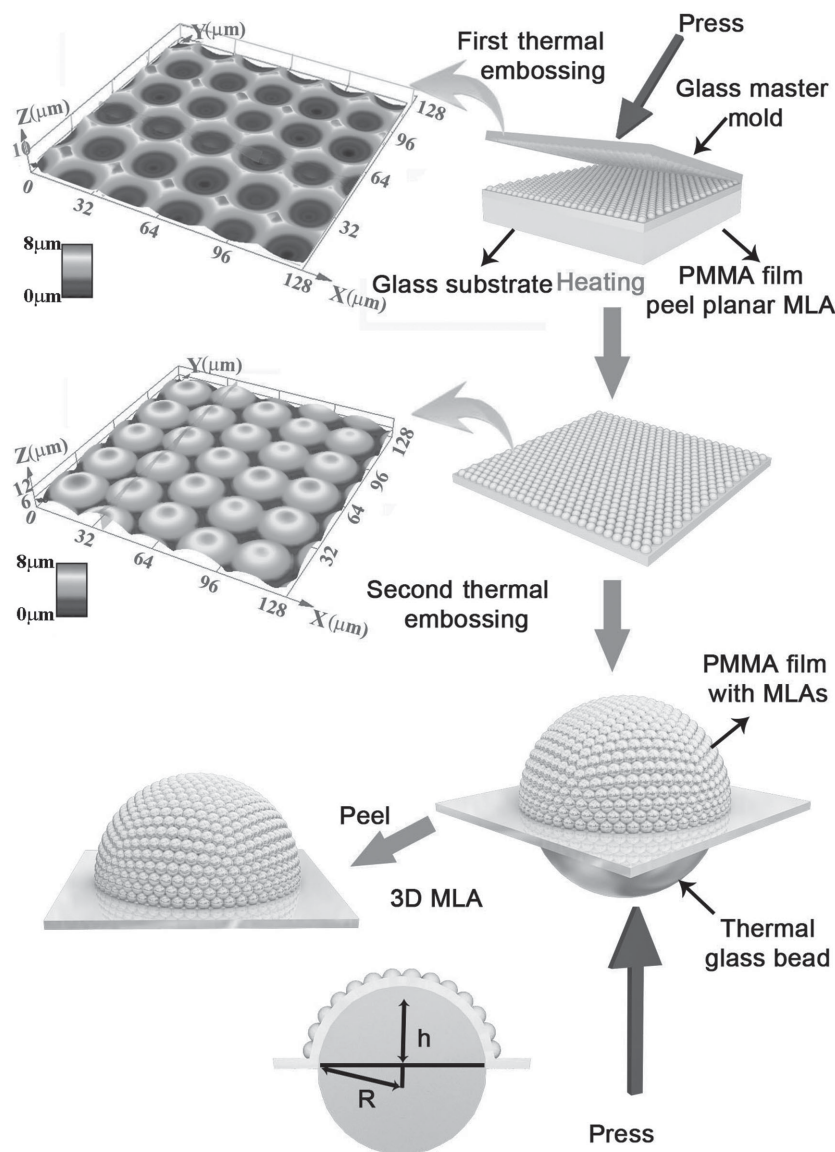


Figure 1. Schematic illustration of the fabrication process for artificial compound eyes by femtosecond laser wet etching and thermal embossing. Insets show 3D morphologies of concave microlenses and replicated convex microlenses, which were measured by laser scanning confocal microscopy.

Moreover, to investigate the surface profile of the convex microlens, we fitted its cross-sectional profile with conic curves. Figure 2d shows the cross-sectional profile of the microlens (line) and the ideal parabola (dots). The theoretical fitting results show that the root-mean-square deviation between the measured cross-sectional profile and the ideal parabola was about 70 nm. It is reasonable to identify the cross-sectional profile as a parabola. Further, the focal length of the microlens with a parabolic surface profile can be calculated as^[34]

$$f = \frac{d^2}{8h_s(n-1)} \quad (1)$$

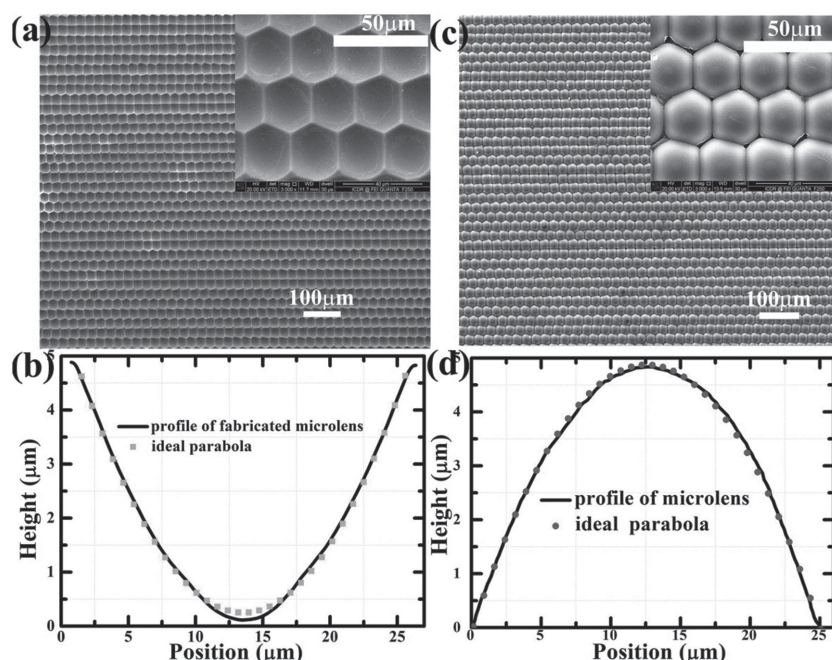


Figure 2. a) SEM image of master mold. b) Cross-sectional profile of a concave microlens mold. c) SEM image of replicated convex microlenses. d) Cross-sectional profile of a replicated convex microlens. Insets in panels (a) and (c) are SEM images at higher magnification. Scale bars in panels (a) and (c) and in their insets are 50 and 100 μm , respectively.

where h_s is the sag height of the microlens, n is the refractive index of PMMA, and d is the aperture diameter of the microlens. Given $d = 24.5 \mu\text{m}$, $h_s = 4.67 \mu\text{m}$, and $n = 1.49$, we have $f = 32.8 \mu\text{m}$.

The planar distributed PMMA MLAs were transformed into a spherical dome by thermomechanical deformation. **Figure 3c** shows an SEM image of the fabricated PMMA dome. The values of diameter and the height of the macrospherical dome were 5 and 1.5 mm, respectively. The structural organizations of the top and side portions are shown at higher magnification

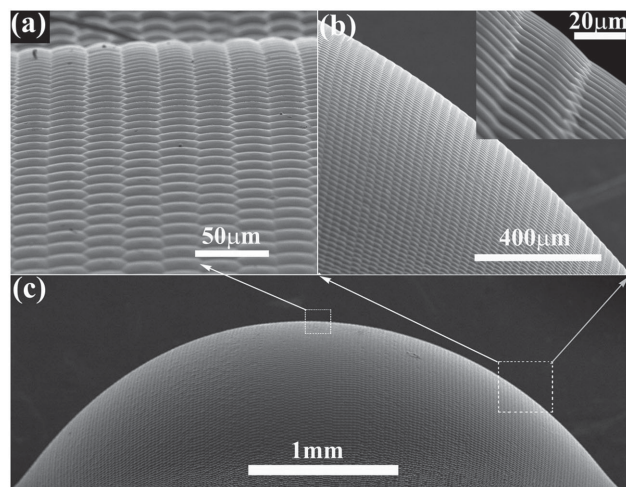


Figure 3. SEM images of structural organization of a) top and b) side portions of the artificial compound eye at high magnification. Insets are high-resolution SEM images. c) SEM image showing overall shape of the eye.

in **Figure 3a,b**, respectively. The convex microlenses were clearly tightly packed on the spherical surface. The high-resolution SEM image in the inset of **Figure 3b** further reveals that the fill factor of the MLA was nearly 100%, which is similar to that of most natural compound eyes.

According to numerical deduction, the theoretical FOV of compound eyes can generally be calculated as

$$\text{FOV} = 2 \arccos\left(\frac{R-h}{R}\right) \quad (2)$$

The FOV was determined from the height (h) and the radius (R) of the macrospherical dome, where R equals to $D/2$. Note that the FOV would increase with increasing h . Nevertheless, the deformation caused by the thermal embossing process strongly limits the value of the height. During the thermomechanical deformation process, the microlenses distributed on a spherical PMMA dome would also deform gradually, including a decrease in the sag height and an increase in the aperture diameter. The maximum deformation of the microlenses, which occurred at the top of the spherical dome,

would increase from 5 to 10 μm when the height of the spherical dome increases from 1.0 to 2.0 mm. In particular, the deformation of the microlenses would vary with the distance from the top of the spherical dome at a certain value of h (**Figure S2**, Supporting Information). In addition, the cross-sectional profiles of the deformational microlenses were measured, and they also fit very well with the ideal parabolic curve (**Figure S3**, Supporting Information). These parabolic shapes of the refractive lenslets are highly desirable for reducing spherical aberration in high-quality optical imaging.^[35]

To demonstrate the imaging performance of the artificial compound eyes, we used a microscopy system comprising a tungsten lamp, a 3D translation stage, an objective lens (Nikon, 10 \times or 20 \times), and a charge-coupled device (CCD) camera. In the measurement, a transport film printed with the letter **F** was placed between the light source and the artificial compound eyes. **Figure 4** shows images of the letter **F** formed by the artificial compound eye. Owing to the nonplanar distribution of the microlens units, the focal points of each unit are not in the same horizontal plane. A clear image from the apex of the artificial compound eye was first acquired (**Figure 4b**), and then the 3D stage was used to move the artificial compound eye closer to the objective lens so that clear images from the outer part can be observed successively from the top to the bottom of the artificial compound eye, as shown in **Figure 4c**. It is noted that every unit of the artificial compound eye can form a sharp image, and the images exhibit high optical uniformity owing to the high quality and uniformity of the ommatidia.

The angular sensitivity function (ASF) is among the most critical parameters that affect the resolving power of artificial compound eyes and can be characterized by measuring the

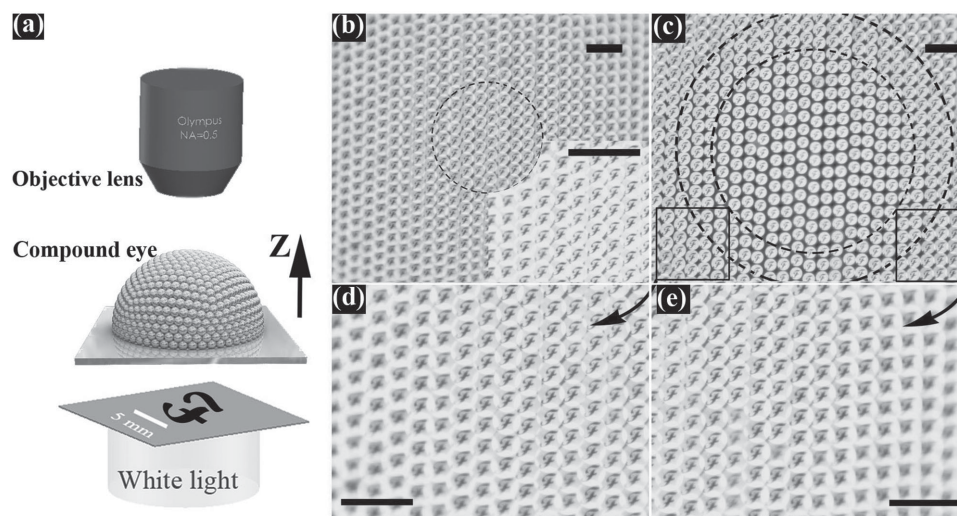


Figure 4. Imaging properties of the artificial compound eyes. a) The schematic diagram of the optical setup. b) Clear images obtained from the apex of the artificial compound eyes. Inset shows magnified image taken through the 20× objective lens. c) Clear images from the outer part (in the annulus) of the artificial compound eye. d, e) Images of lower left and lower right zones in panel (c), respectively, at higher magnification. Scale bar: 100 μm .

relative intensity of the incident light at the distal end of each ommatidium¹¹. **Figure 5a** shows the experimental setup used to measure the ASF of a single ommatidium. A laser with a wavelength of 632.8 nm was used as a light source. Because the omnidirectionally arranged ommatidia are pointed in different directions, the incident laser would be coupled into

each ommatidium with a different coupling efficiency. Then, the distributions of the output laser pattern, which was a confocal image on the xy plane, were captured by a CCD camera (Figure 5b). The cross-sectional intensity distribution along the line ll' is also shown at the bottom of Figure 5b. Furthermore, to acquire the ASF of a single ommatidium, the relative

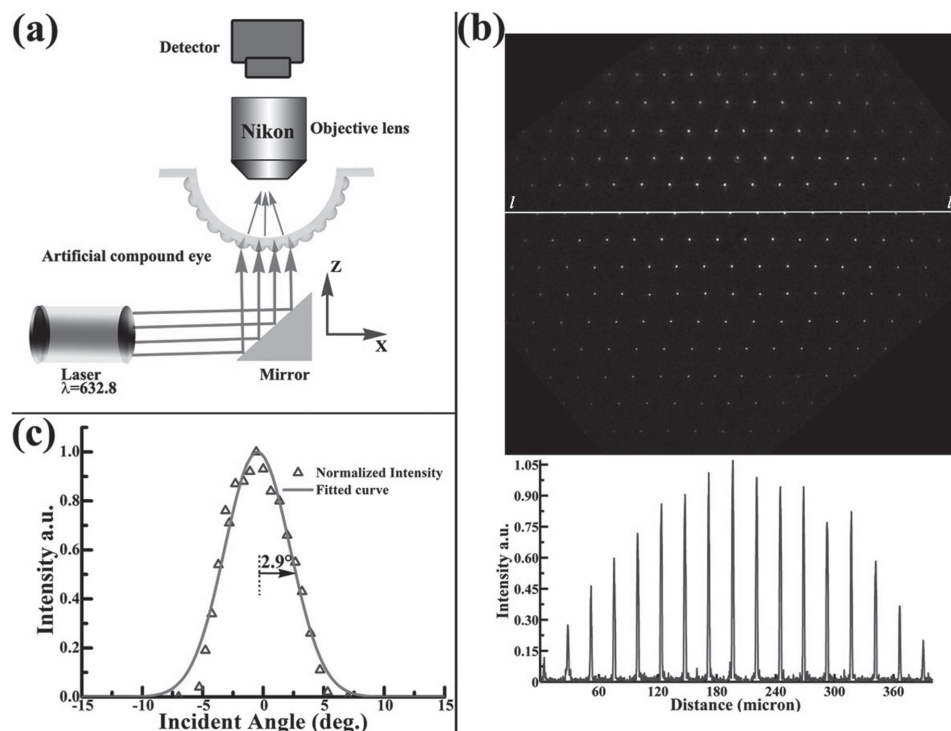


Figure 5. a) Schematic diagram of experimental setup for measuring the ASF of a single ommatidium. b) Optical microscopy confocal images of the artificial compound eye illuminated by a normally incident laser at 632.8 nm and the normalized intensity distribution obtained along line ll' . c) ASF of the artificial compound eye.

intensities of the peaks, which represent the sensitivity of the ommatidia to different incident angles, were obtained using a photodetector with a pinhole to scan the intensity in 5 μm steps; the results are plotted versus the incident angle and approximately fitted with a Gaussian distribution (Figure 5c). Note that the intensity decreases to 0.5 when the laser was incident at a tilt angle of 2.9° . Hence, the acceptance angle, or the full width at half-maximum (FWHM) of the ASF, is 5.8° . Further, this value is wider than the interommatidial angle ($\Delta\phi = 0.57^\circ$, $\Delta\phi = d/R$, where d is the center-to-center spacing between two adjacent ommatidia, and R is the diameter of the eye), so optical overlap between contiguous ommatidia would occur. However, this optical crosstalk might be reduced by arranging the distribution of the microlenses and introducing a self-written waveguide.^[11,29]

According to Equation (1), for $h = 1.5$ mm and $R = 2.5$ mm, we can calculate the theoretical FOV of the artificial compound eye as 132.8° . Moreover, to characterize the large FOV of the artificial compound eyes experimentally, a measurement system equipped with a laser source (wavelength, 632.8 nm), an objective lens (magnification, 20 \times), and a CCD camera was set up. The laser could be adjusted to irradiate the artificial compound eye at different incident angles (θ). Figure 6a–c shows CCD images of the laser patterns through the ommatidia for θ equal to 0, 30, and 60° , respectively. The focal spots remain orbicular and clear regardless of the incident angle of the laser. This result confirmed that the FOV of the artificial compound eye was 120° . More importantly, no obvious distortions could be observed in the images of the focal spots. Nevertheless, we should recognize that the experimental value of the FOV ($\approx 125^\circ$) was less than the theoretical value ($\approx 132.8^\circ$). For $h = 2$ mm, the theoretical FOV of the artificial compound eye is 156.9° . The experimental measured FOV is about 140° and there are also no obvious distortions (Figure S4, Supporting Information). When the incoming laser angle was $\pm 75^\circ$, the obtained focal spots began to appear slight distortions.

Though the FOV of nearly 150° might be a little less than some natural compound eyes, which are even close to 180° , artificial compound eyes with wider FOV could be fabricated by setting a larger macrobase height in our experiments. In addition, artificial compound eyes with different macrobase heights were fabricated, and their FOV values were investigated (Figure S5, Supporting Information). Their FOVs were slightly less than the theoretical value owing to deformation of the PMMA membrane during the second thermal embossing process.

Furthermore, to quantify the distortion rate of the artificial compound eye, the intensity distribution of the focal spots along the x and y axes were extracted from the microscope images. Figure 6d shows the cross-sectional intensity distribution of a single focal spot along the x and y axes for θ equal to 0° . The intensity distributions along the two directions were obviously roughly identical, indicating that the ommatidia exhibit good focusing ability. In addition, for $\theta = 0, 30$, and 60° , the intensity distributions of a single focal spot were characterized, and the x -direction (Figure 6e) and y -direction (Figure 6f) intensity distributions were compared. The FWHM intensities were 1.7 ± 0.1 μm (x axis) and 1.6 ± 0.3 μm (y axis). We suggest that the small fluctuations in spot size along the x or y axis might be caused by nonnormal incidence of the laser. Hence, the FWHM could be considered as constant regardless of the incident angle of the laser. This result demonstrates that the artificial compound eyes exhibit a wide FOV without imaging distortion.

It is noted that optoelectronics components integration, such as silicon photodiodes or photodetector, is significant for practical applications of the artificial compound eyes. Though the arrangement of our planar microlens array was nonperiodic, the location information of every microlens could be easily acquired by their focusing spots, which could be used to produce artificial underlying “photoreceptive” structure to match the microlens pattern. Moreover, Rogers et al. have fabricated hemispherical silicon photodiodes and combined simple microlens array with them to realize wide FOV digital cameras.^[9,10] Similarly, this method

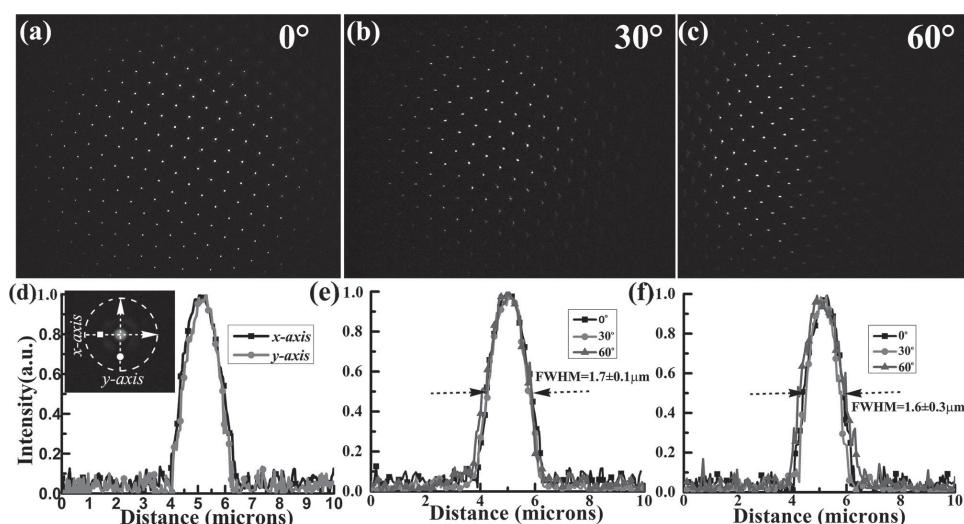


Figure 6. Experimentally observed wide FOV of the artificial compound eyes. a–c) Output patterns of the artificial compound eyes irradiated by a laser at incident angles of 0, 30, 60° , respectively. d) Comparison of intensity distribution along x and y axes for θ equal to 0° . Inset is a microscope image of a single focal spot. e, f) Comparison of x - and y -direction intensity distributions under incident angles of 0, 30, 60° .

could be easily applied to integrate our artificial compound eyes with electronic components for practical applications.

3. Conclusions

In conclusion, high-quality artificial compound eyes were realized using a high-throughput method that combines sp-FLWE with thermal embossing and that exhibits tremendous potential for large-scale industrial production. Our artificial compound eyes are morphologically as well as functionally close to natural dragonfly compound eyes (Table S1, Supporting Information). They possess ommatidia that differ slightly in shape and size in a single eye and have an average diameter of 24.5 μm . Thousands of ommatidia, about 30 000 in our artificial compound eyes, are packed over a spherical base with a fill fraction of 100%. The FOV of a single artificial compound eye reaches 140° and can exceed 180° when a pair of eyes is assembled, which is similar to that of natural compound eyes. The compound eye weighs only 67 mg overall, so it can be integrated into other systems without introducing excessive weight. Furthermore, comparisons among the focal spots at different incident angles revealed distortion-free imaging by the artificial compound eye.

4. Experimental Section

Master Mold Fabrication: The master mold is a $20 \times 20 \times 2 \text{ mm}^3$ commercial silica glass (BK7) sheet with both sides polished. The laser was generated by a regeneratively amplified Ti:sapphire laser system (Coherent Libra-usp-he) with a pulse duration of 50 fs, central wavelength of 800 nm, and repetition rate of 1 KHz; it was focused by an objective lens (Nikon, 50 \times , N.A. \approx 0.5) before striking the surface of the substrate normally. The intensity of each pulse was set to 5.0 μJ . The etching solution is HF with a volume fraction of 5%, which was prepared by mixing a commercial HF solution of 40% v/v with deionized water. The laser-irradiated glass substrates were immersed in the HF solution for about 20 min at room temperature.

Preparation for PMMA Slice: The PMMA material used here consisted of conventional commercial particles with a single-particle diameter of roughly several millimeters. PMMA particles (4 g) were dissolved in acetone (20 mL) in an ultrasonic water bath. The prepared solution was spin-coated at 100 rpm on a glass slide and set aside for 24 h at room temperature. Then, a PMMA slice with a thickness of about 350 μm could be peeled off the glass substrate. These slices were generally not smooth because they contained a few bubbles. An additional process was essential to acquire smooth PMMA slices. A smooth PMMA slice with a thickness of 250 μm was acquired by a hot-press process at 120 °C, in which the prepared PMMA slice was sandwiched between two smooth glass slices.

Replication of Convex MLAs: The master mold was placed in conformal contact with a PMMA slice on a glass substrate and heated by a heating system with an automatic thermostat. Further, an increasing external pressure was applied on the other side of the master mold. The thickness of the PMMA film was 250 μm . The temperature was set to 95 °C considering the glass transition temperature of PMMA, which is about 105 °C. In this process, the glass substrate was essential for the uniformity of the fabricated convex MLA because it evenly distributed the heat and force applied to the PMMA film. Then, while the pressure was maintained, slow cooling was applied to relax the internal stress and avoid scattering centers, which would be detrimental for optical applications. Finally, the film was peeled off of the master mold using an ultrasonic water bath.

3D Fabrication: A glass bead was heated to 100 °C and slowly pressed into the surface of a PMMA film without MLA patterning. Hence, the height of the fabricated PMMA dome, h , which was equal to the shift in the glass bead's position, could be easily controlled. Finally, the spherical PMMA dome was peeled off of the glass bead until it dropped to room temperature.

Supporting Information

Supporting Information is available from the Wiley Online Library or from the author.

Acknowledgements

This work was supported by the National Science Foundation of China under the Grant Nos. 51335008, 61275008, and 61475124, the Special-funded Program on National Key Scientific Instruments and Equipment Development of China under the Grant No. 2012YQ12004706, and the Collaborative Innovation Center of Suzhou Nano Science and Technology. The SEM work was done at International Center for Dielectric Research (ICDR), Xi'an Jiaotong University; the authors also thank Juan Feng for her help in using SEM. Moreover, the authors acknowledge Dr. Hewei Liu for valuable discussion.

Received: November 18, 2015

Revised: December 29, 2015

Published online: February 8, 2016

- [1] R. M. Olberg, R. C. Seaman, M. L. Coats, A. F. Henry, *J. Comp. Physiol.* **2007**, 193, 685.
- [2] R. M. Olberg, *J. Comp. Physiol.* **1981**, 141, 327.
- [3] A. C. Zelhof, R. W. Hardy, A. Becker, C. S. Zuker, *Nature* **2006**, 433, 696.
- [4] W. H. Miller, G. D. Bernard, F. L. Allen, *Science* **1968**, 162, 760.
- [5] A. W. Snyder, D. G. Stavenga, S. B. Laughlin, *J. Comp. Physiol.* **1977**, 116, 183.
- [6] M. F. Land, *Nature* **1980**, 287, 681.
- [7] L. P. Lee, R. Szema, *Science* **2005**, 310, 1148.
- [8] C. C. Huang, X. D. Wu, H. W. Liu, B. Aldalali, J. A. Rogers, H. R. Jiang, *Small* **2014**, 10, 3050.
- [9] H. C. Ko, M. P. Stoykovich, J. Song, V. Malyarchuk, W. M. Choi, C. J. Yu, J. B. Geddes, J. Xiao, S. Wang, Y. Huang, J. A. Rogers, *Nature* **2008**, 454, 748.
- [10] Y. M. Song, Y. Xie, V. Malyarchuk, J. Xiao, I. Jing, K. J. Choi, Z. Liu, H. Park, C. Lu, R. H. Kim, R. Li, R. K. B. Crozier, Y. Huang, J. A. Rogers, *Nature* **2013**, 497, 95.
- [11] K. H. Jeong, J. Kim, L. P. Lee, *Science* **2006**, 312, 557.
- [12] D. M. Keum, H. J. Jung, K. H. Jeong, *Small* **2012**, 14, 2169.
- [13] H. Kawano, T. Okamoto, H. Nakajima, S. Takushima, Y. Toyoda, S. Yamanaka, T. Funakura, K. Yamagata, T. Matsuzawa, T. Kunieda, T. Minobe, *Opt. Express* **2014**, 15, 18010.
- [14] M. C. Ma, F. Cao, Z. Guo, K. Wang, *Appl. Opt.* **2014**, 53, 1166.
- [15] L. Wang, H. Liu, W. Jiang, R. Li, F. Li, Z. Yang, L. Yin, Y. Shi, B. Chen, *J. Mater. Chem. C* **2015**, 3, 5896.
- [16] Z. W. Li, J. L. Xiao, *J. Appl. Phys.* **2015**, 117, 014904.
- [17] D. G. Beersma, D. G. Stavenga, J. W. Kuiper, *J. Comp. Physiol.* **1975**, 102, 305.
- [18] J. W. Duparré, F. C. Wippermann, *Bioinspiration Biomimetics* **2006**, 1, R1.
- [19] D. Zhu, C. Li, X. Zeng, H. R. Jiang, *Appl. Phys. Lett.* **2010**, 96, 081111.

- [20] H. Liu, F. Chen, Q. Yang, P. Qu, S. He, X. Wang, J. Si, J. X. Hou, *Appl. Phys. Lett.* **2012**, 100, 133701.
- [21] C. Armet-Kibel, I. A. Meinertzhagen, *J. Comp. Physiol.* **1983**, 151, 285.
- [22] E. P. Meyer, T. Labhart, *Cell Tissue Res.* **1993**, 272, 17.
- [23] K. Arikawa, D. G. Stavenga, *J. Exp. Biol.* **1997**, 200, 2501.
- [24] T. F. Lau, E. M. Gross, V. B. Meyer-Rochow, *Eur. J. Entomol.* **2007**, 104, 459.
- [25] T. E. Sherk, *J. Exp. Zool.* **1978**, 203, 61.
- [26] T. E. Sherk, *J. Exp. Zool.* **1978**, 203, 183.
- [27] T. H. Goldsmith, *Q. Rev. Biol.* **1990**, 65, 281.
- [28] D. Radtke, J. Duparré, U. D. Zeitner, A. Tünnermann, *Opt. Express* **2007**, 15, 3067.
- [29] D. Wu, J. Wang, L. Niu, X. Zhang, S. Wu, Q. Chen, L. Lee, H. Sun, *Adv. Opt. Mater.* **2014**, 2, 751.
- [30] D. Stumpf, U. D. Zeitner, *Appl. Phys. B* **2014**, 115, 371.
- [31] E. P. Chan, A. J. Crosby, *Adv. Mater.* **2006**, 18, 3238.
- [32] F. Chen, Z. Deng, Q. Yang, *Opt. Lett.* **2014**, 39, 606.
- [33] Z. Deng, Q. Yang, F. Chen, H. Bian, J. Yong, G. Du, Y. Hu, X. Hou, *IEEE Photonics Technol. Lett.* **2014**, 26, 2086.
- [34] P. Nussbaum, R. Völkel, H. P. Herzig, M. Eisner, S. Haselbeck, *Pure Appl. Opt.* **1997**, 6, 617.
- [35] D. Wu, S. Z. Wu, L. G. Niu, Q. D. Chen, R. Wang, J. F. Song, H. H. Fang, H. B. Sun, *Appl. Phys. Lett.* **2010**, 97, 031109.